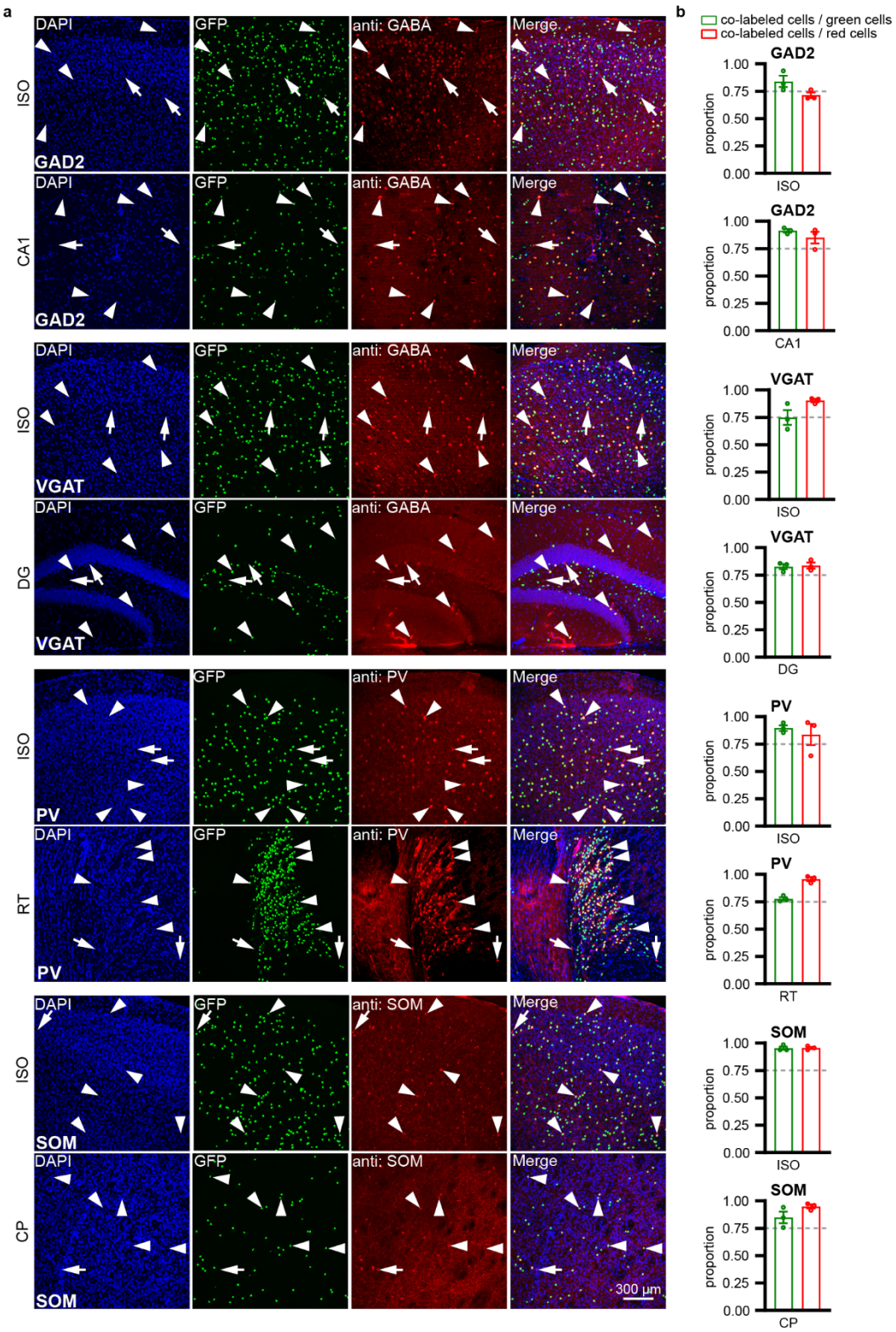

Supplementary Fig. 1 | Immunohistochemical validation of four types of GABAergic neurons

(a) Representative images from two brain regions for each neuron type are shown. Arrows indicate cells that are co-labeled in both red and green channels, representing cells expressing both H2B-GFP and the corresponding antibody. Arrowheads indicate cells labeled only by the antibody without H2B-GFP expression. Scale bar, 300 μm.

(b) Proportions of co-labeled cells relative to GFP-labeled cells (green) and antibody-labeled cells (red).

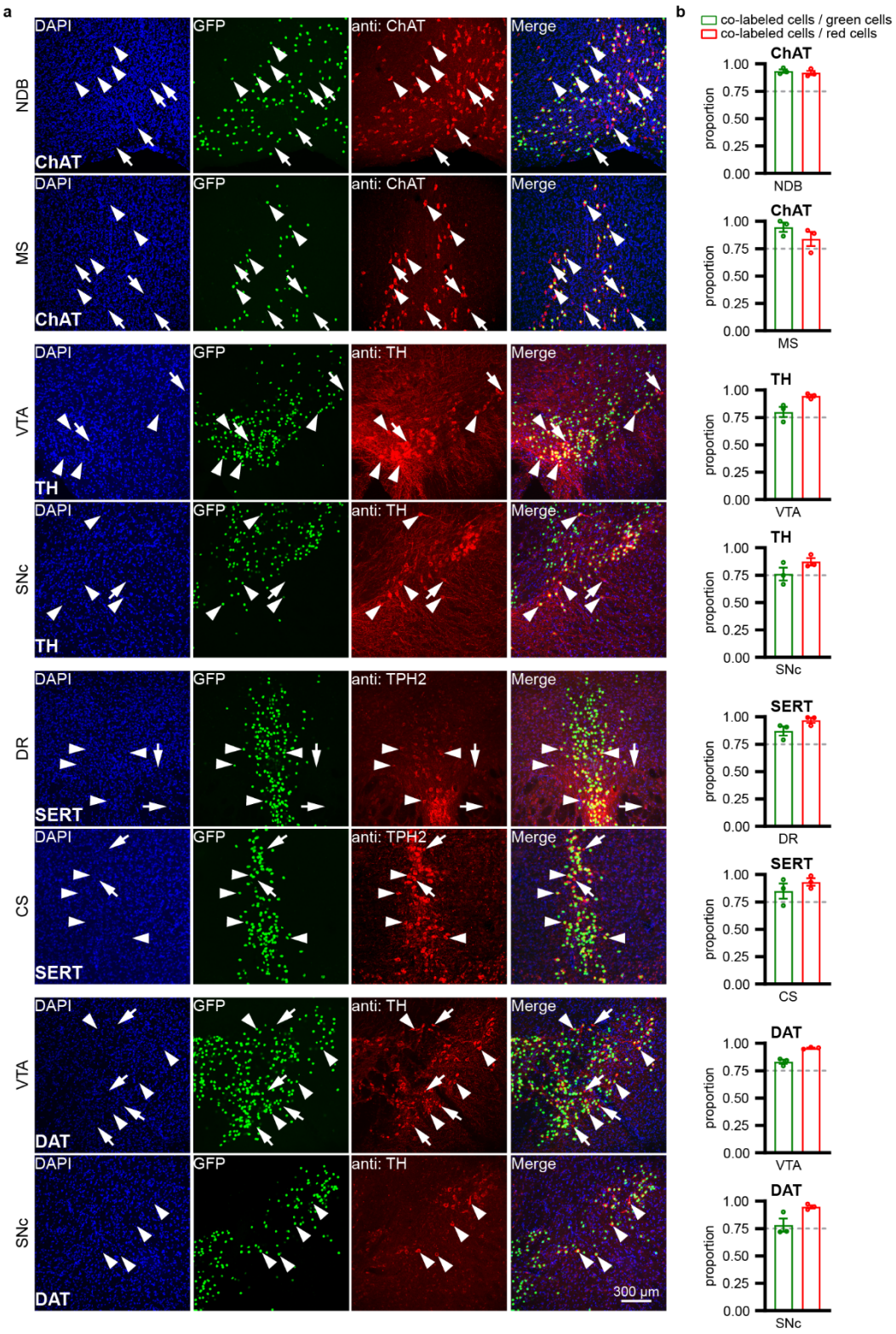

Supplementary Fig. 2 | Immunohistochemical validation of four types of modulatory neurons

(a) Representative images from two brain regions for each neuron type are shown. Arrows indicate cells that are co-labeled in both red and green channels, representing cells expressing both H2B-GFP and the corresponding antibody. Arrowheads indicate cells labeled only by the antibody without H2B-GFP expression. Scale bar, 300 µm.

(b) Proportions of co-labeled cells relative to GFP-labeled cells (green) and antibody-labeled cells (red).

a

Sampling observation for cell counting

ID	MouseLine	Precision	Recall	F1 Score	CellNumber
1	Scnn1a	1.000	1.000	1.000	11
2	GAD2	1.000	0.929	0.963	14
3	Emx1	1.000	0.909	0.952	33
4	GAD2	0.980	1.000	0.990	49
5	Scnn1a	0.980	0.980	0.980	50
6	Cart	0.980	0.962	0.971	52
7	DAT	0.942	0.875	0.907	56
8	PV	1.000	1.000	1.000	57
9	GAD2	0.984	1.000	0.992	61
10	SERT	0.967	0.937	0.952	63
11	GAD2	0.950	0.962	0.956	79
12	SERT	0.988	0.976	0.982	84
13	Cart	1.000	1.000	1.000	87
14	TH	0.979	0.959	0.969	97
15	Thy1	0.872	0.913	0.892	104
16	DAT	1.000	0.991	0.995	109
17	VGLUT2	0.981	0.955	0.968	110
18	VGLUT2	0.991	0.983	0.987	116
19	Emx1	1.000	0.828	0.906	116
20	VGLUT2	0.938	0.861	0.897	122
21	VGLUT2	0.966	0.935	0.950	123
22	Cart	1.000	0.984	0.992	124
23	VGLUT2	0.972	0.972	0.972	142
24	Cart	0.993	0.987	0.990	152
25	VGLUT2	0.993	0.987	0.990	153
26	Thy1	0.977	0.955	0.966	177
27	Cart	0.989	0.972	0.981	181
28	Thy1	0.955	0.914	0.934	185
29	Emx1	0.989	0.963	0.976	189
30	VGLUT2	0.989	0.979	0.984	192
31	VGLUT2	0.974	0.950	0.962	201
32	Cart	0.943	0.866	0.903	209
33	VGLUT2	0.986	0.981	0.984	215
34	VGAT	0.981	0.963	0.972	216
35	VGAT	0.976	0.932	0.953	220
36	Thy1	0.972	0.942	0.957	223
37	VGLUT2	0.987	0.978	0.982	228
38	Thy1	0.955	0.933	0.944	252
39	Emx1	0.992	0.981	0.986	258
40	DAT	0.984	0.977	0.981	258
41	VGLUT2	0.940	0.908	0.924	260
42	Thy1	0.986	0.975	0.980	283
43	VGAT	0.966	0.932	0.949	309
44	VGLUT2	0.929	0.903	0.916	321
45	VGLUT2	0.978	0.960	0.969	323
46	Camk2a	0.940	0.889	0.914	333
47	Emx1	0.971	0.963	0.967	349
48	Cart	0.979	0.958	0.968	382
49	Emx1	0.982	0.972	0.977	390
50	Emx1	0.980	0.978	0.979	407
51	VGAT	0.966	0.920	0.943	564
52	Emx1	0.901	0.873	0.887	806
53	Camk2a	0.906	0.801	0.850	946
54	VGLUT2	0.959	0.918	0.938	1124
Mean		0.972	0.947	0.959	225
Min		0.872	0.801	0.850	11
Q1		0.966	0.922	0.945	99
Q2		0.980	0.961	0.969	183
Q3		0.989	0.979	0.982	260
Max		1.000	1.000	1.000	1124

b

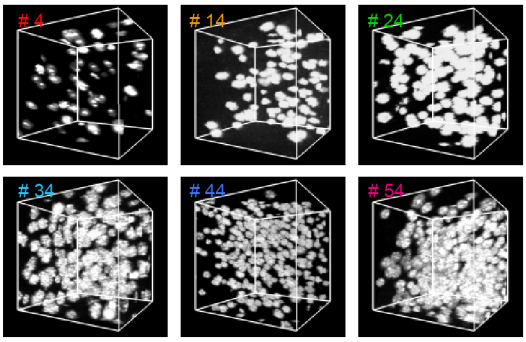

c

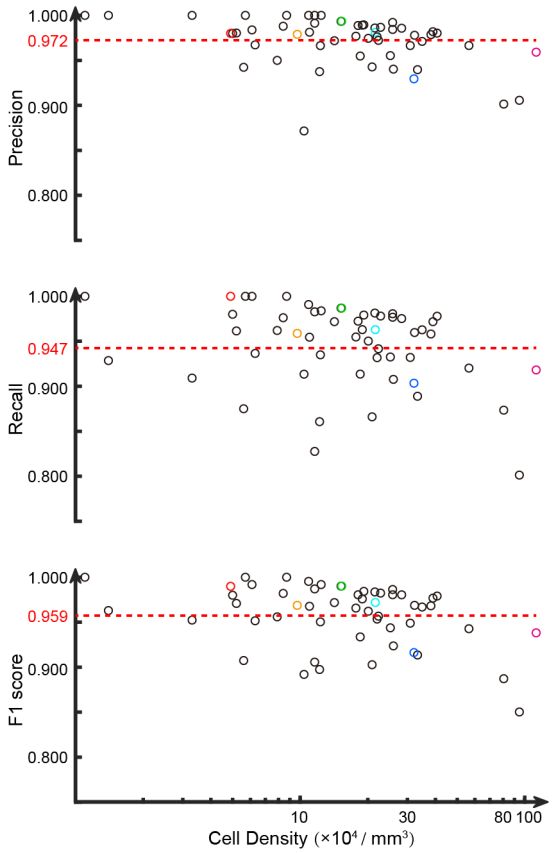

Supplementary Fig. 3 | Evaluation of automatic cell counting

(a) Sampling observations for cell counting. A total of 54 three-dimensional image blocks, each measuring 100 µm × 100 µm × 100 µm, were analyzed and arranged in ascending order based on their cell counts. The mean, minimum, first quartile (Q1), median (Q2), third quartile (Q3), and maximum values of precision, recall, F1 score, and cell counts are displayed. Samples are color-coded according to neuronal density.

(b) Representative image blocks with varying cell densities corresponding to the selected samples in (a). The Sample ID for each block is shown in the top-left corner.

(c) Visualization of precision, recall, and F1 scores for the data blocks in (a) across different cell densities. Red dashed lines indicate the mean values for each evaluation metric. Colored circles represent evaluation data corresponding to the blocks shown in (b).

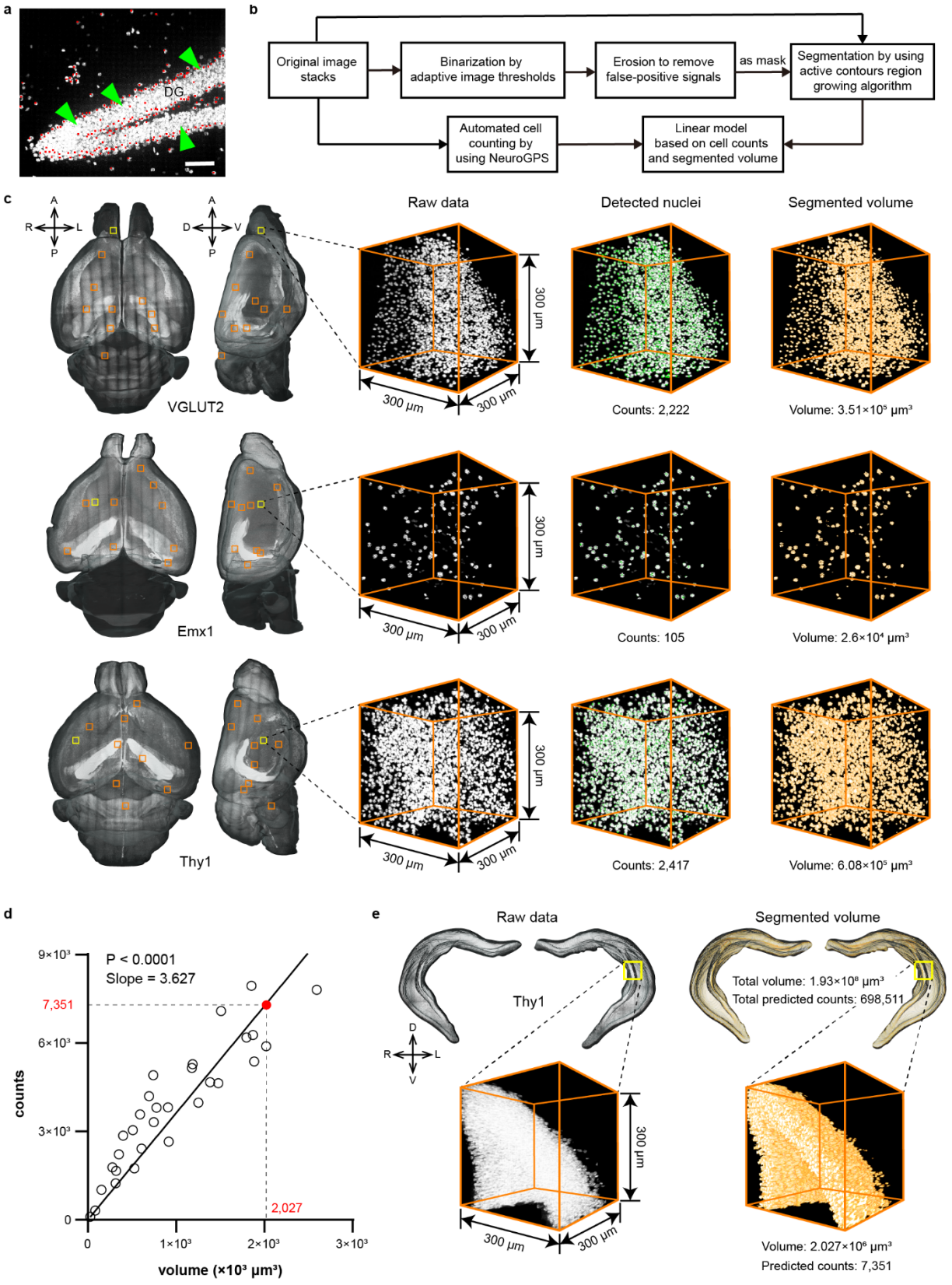

Supplementary Fig. 4 | Estimating the number of nuclei in the DG

(a) Automatic detection of Thy1$^+$ nuclei (red dots) in the DG using NeuroGPS. Green arrows indicate regions with nuclei densities too high to be automatically detected. The image represents a maximum intensity projection along the z-axis with a thickness of 20 µm.

(b) Flowchart illustrating the development of a linear model to estimate the number of nuclei in

regions with extremely high densities.

(c) 3D visualization of whole-brain datasets showing regions with extremely dense nuclei in the DG (first column) and representative data blocks from other brain regions. The second column shows raw data, the third column displays detected nuclei, and the fourth column presents the segmented volume for regions with relatively less dense nuclei that can be automatically detected.

(d) Linear model for estimating the number of nuclei in data blocks with known volumes. The red dot represents the data block shown in (e).

(e) 3D visualization of $Thy1^+$ nuclei in the DG. The left panel shows raw data, while the right panel displays a representative data block and its corresponding segmented volume. Predicted counts of $Thy1^+$ nuclei in the DG and the selected block are indicated below the images.

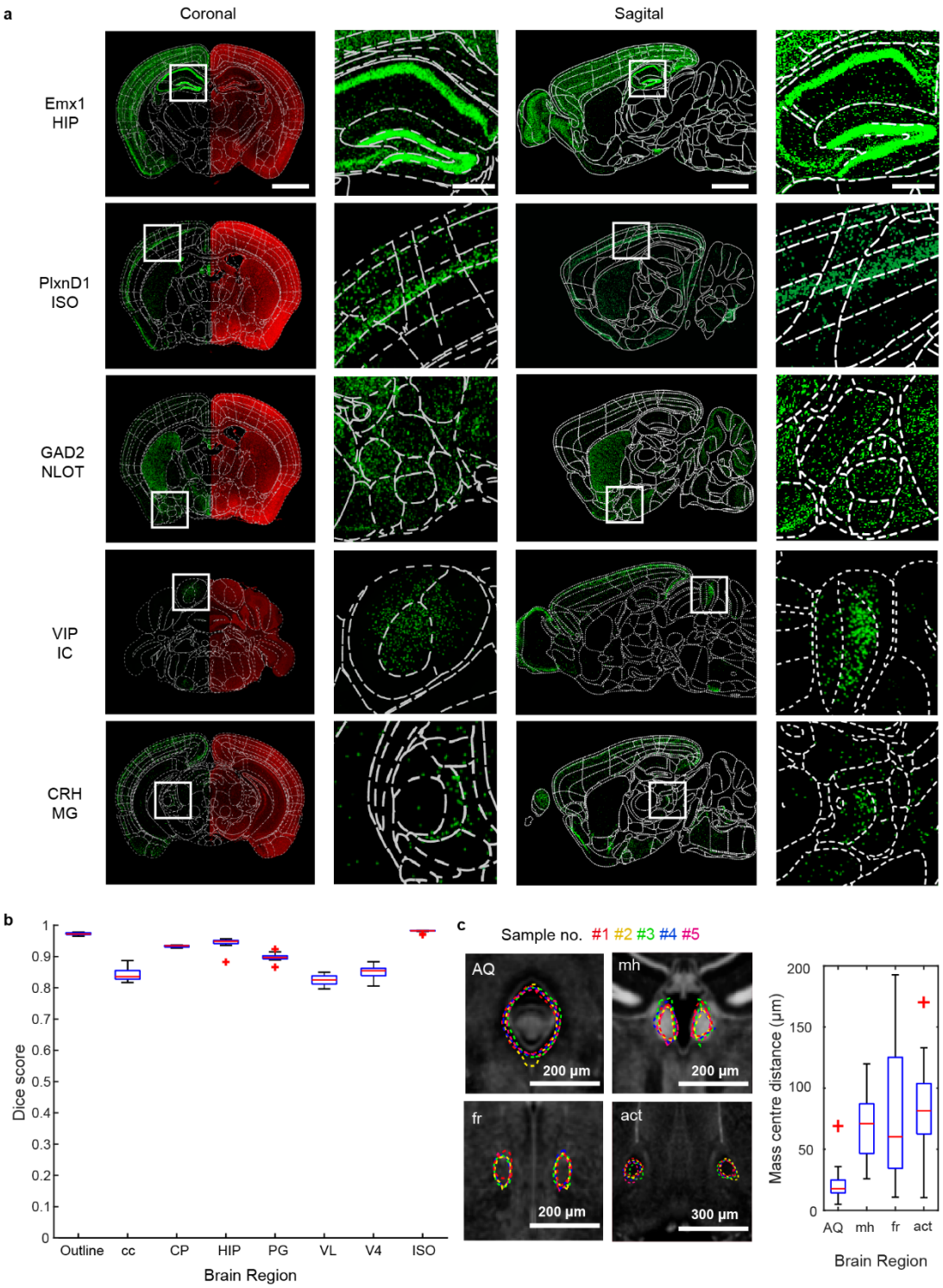

Supplementary Fig. 5 | Evaluation of whole-brain registration

(a) Representative coronal and sagittal slices from registered datasets, with white dashed lines indicating anatomical borders defined by CCFv3. The brain regions selected for magnified views are shown on the left. Images are presented as maximum intensity projections along the z-axis with a thickness of 10 μm. Scale bars, 2 mm for coronal and sagittal slices; 500 μm for magnified views.

(b) Registration accuracy across different brain regions evaluated using Dice scores.

(c) Nuclei-level evaluation of registration accuracy. The outlines (dashed lines) of registered nuclei

from different samples (represented by different colors) are overlaid on coronal images of the CCFv3 averaged mouse brain. The boxplot (right) shows the distances between the mass centers of registered nuclei and their corresponding nuclei in CCFv3.

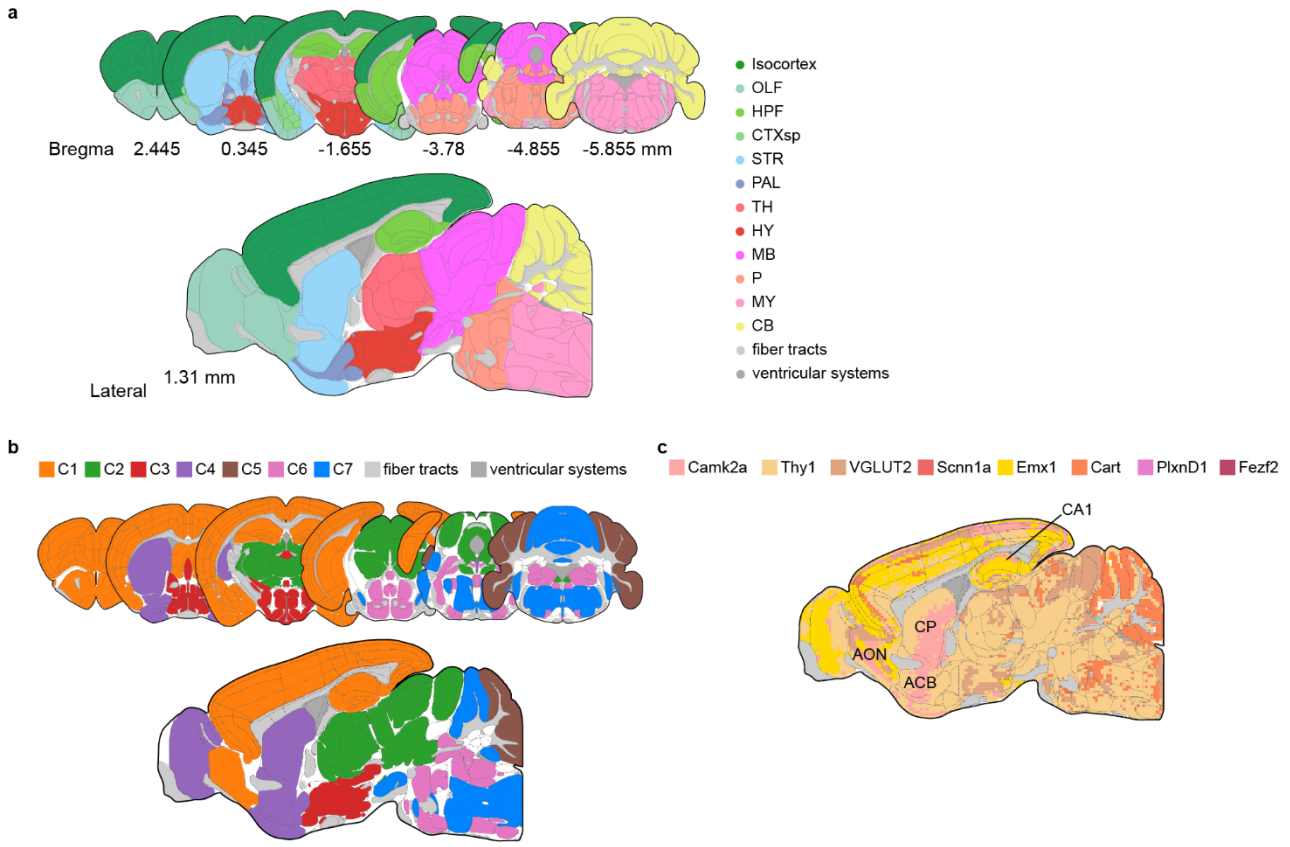

Supplementary Fig. 6 | Spatial organization patterns of 8 types of glutamatergic neurons

(a) Coronal slices (top) and a sagittal slice (bottom) with anatomical boundaries of brain regions adapted from CCFv3. The distances from Bregma for each coronal slice and from the midline for the sagittal slice are indicated below, with all dimensions in millimeters.

(b) Mapping of 134 clustered anatomical regions onto the CCFv3. Clustering is based on the density distributions of 8 types of glutamatergic neurons across brain regions.

(c) Cubic density analysis of the 8 glutamatergic neuron types. Each cube is assigned a type corresponding to the neuron type with the highest density within it.

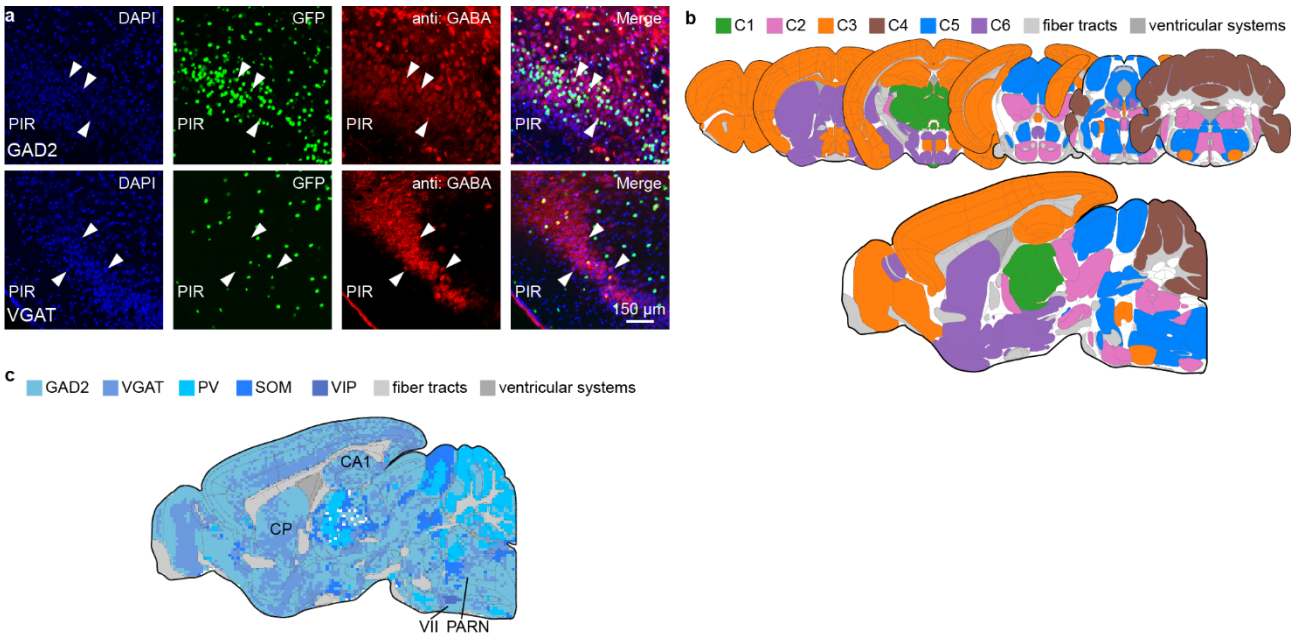

Supplementary Fig. 7 | Spatial organization patterns of 5 types of GABAergic neurons

(a) Immunohistochemical staining of the piriform cortex (PIR) in GAD2-Cre;*LSL-H2B-GFP (top) and VGAT-Cre;*LSL-H2B-GFP (bottom) mice. Scale bar, 150 μm.

(b) Mapping of 134 clustered anatomical regions onto CCFv3. Clustering is based on the density distributions of 5 types of GABAergic neurons across brain regions.

(c) Cubic density analysis of the 5 GABAergic neuron types. Each cube is assigned a type corresponding to the neuron type with the highest density within it.

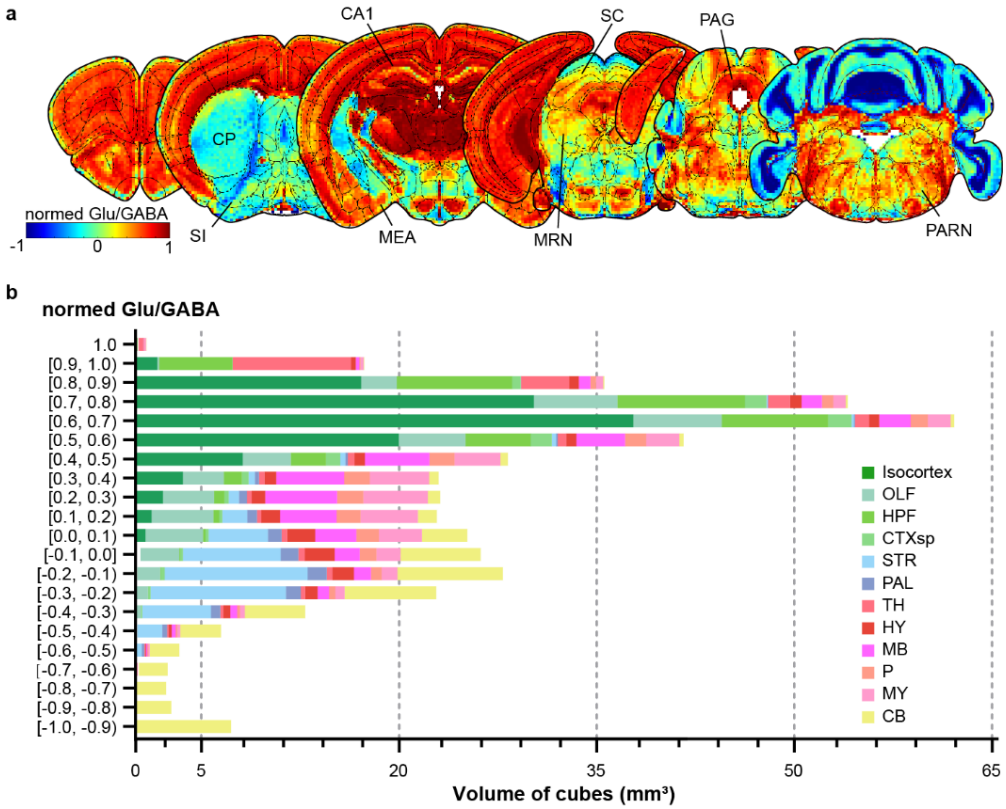

Supplementary Fig. 8 | Cubic normed Glu/GABA in the whole mouse brain

(a) Coronal heatmaps showing the distribution of the normed Glu/GABA ratio across the entire mouse brain, based on cubic normed Glu/GABA ratio analysis at a resolution of 100 µm × 100 µm × 100 µm. (b) Volume of cubes within each range of normed Glu/GABA ratios. Colors represent the 12 brain regions to which the cubes belong.

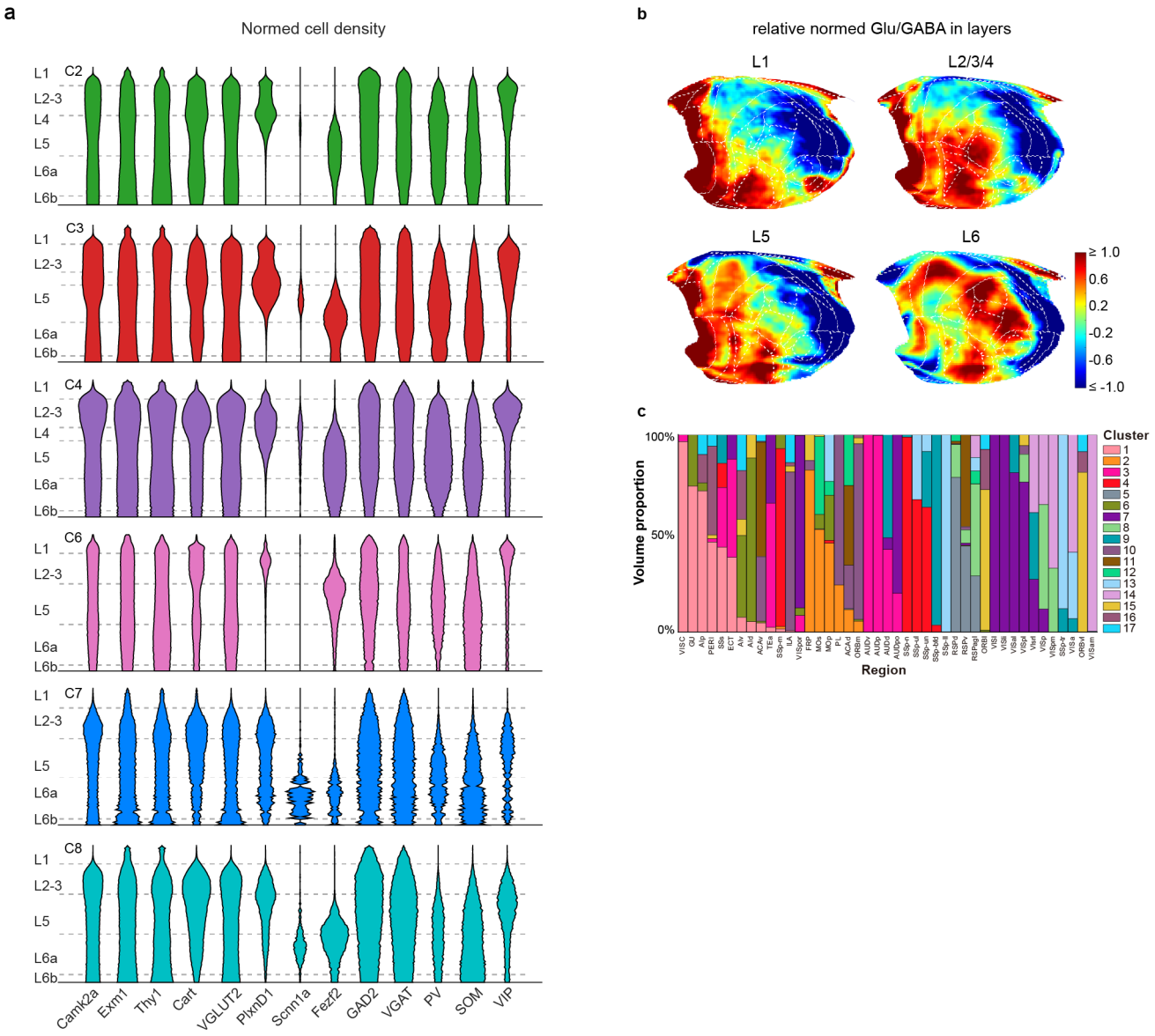

Supplementary Fig. 9 | Molecularly defined modules in the isocortex

(a) Normalized density of 13 neuron types across cortical depth (right) for clusters C2, C3, C4, C6, C7, and C8 shown in Fig. 4a. The density at each cortical column location is calculated as the logarithm of the mean density across all brain regions within each cluster, followed by type-specific normalization.

(b) Heatmaps displaying the relative normalized Glu/GABA ratio in cortical layers 1, 2/3/4, 5, and 6 in a flatmap view.

(c) Volume proportions of 17 clusters across 43 isocortical brain regions.

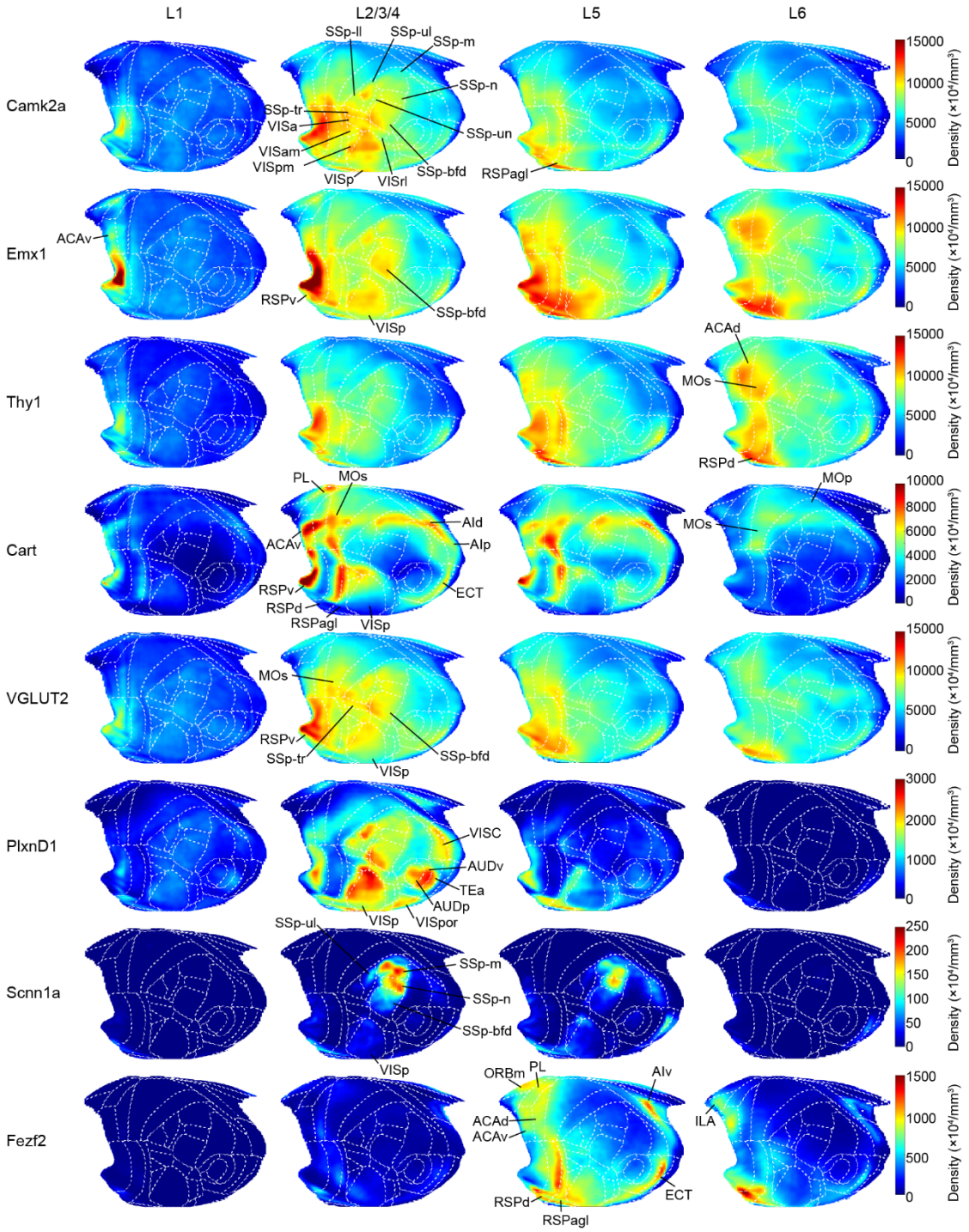

Supplementary Fig. 10 | Density distribution of 8 glutamatergic neuron types in the isocortex

Heatmaps showing the density distribution of 8 types of glutamatergic neurons in the isocortex, visualized in a flatmap view. Distinct colorbars are applied to each neuron type for enhanced visualization.

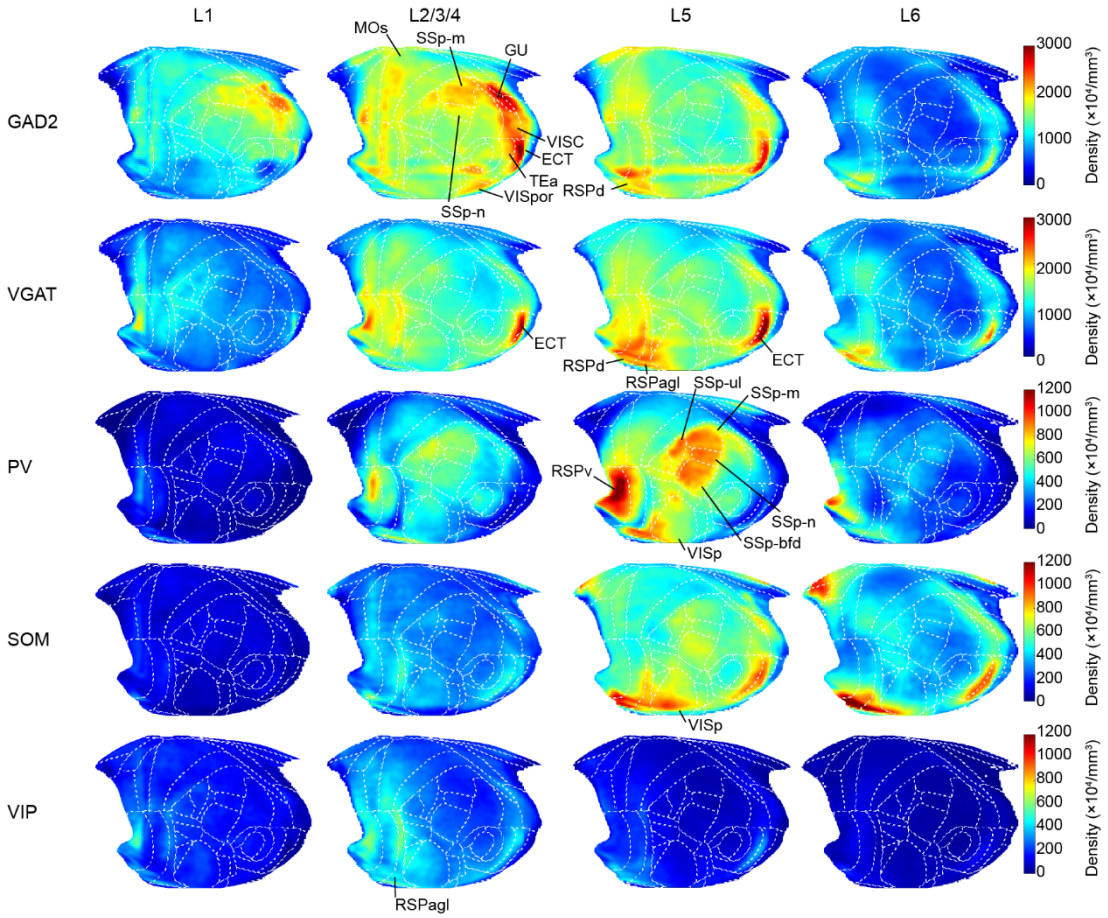

Supplementary Fig. 11 | Density distribution of 5 GABAergic neuron types in the isocortex

Heatmaps showing the density distribution of 5 types of GABAergic neurons in the isocortex, visualized in a flatmap view. Distinct colorbars are applied to each neuron type for enhanced visualization.

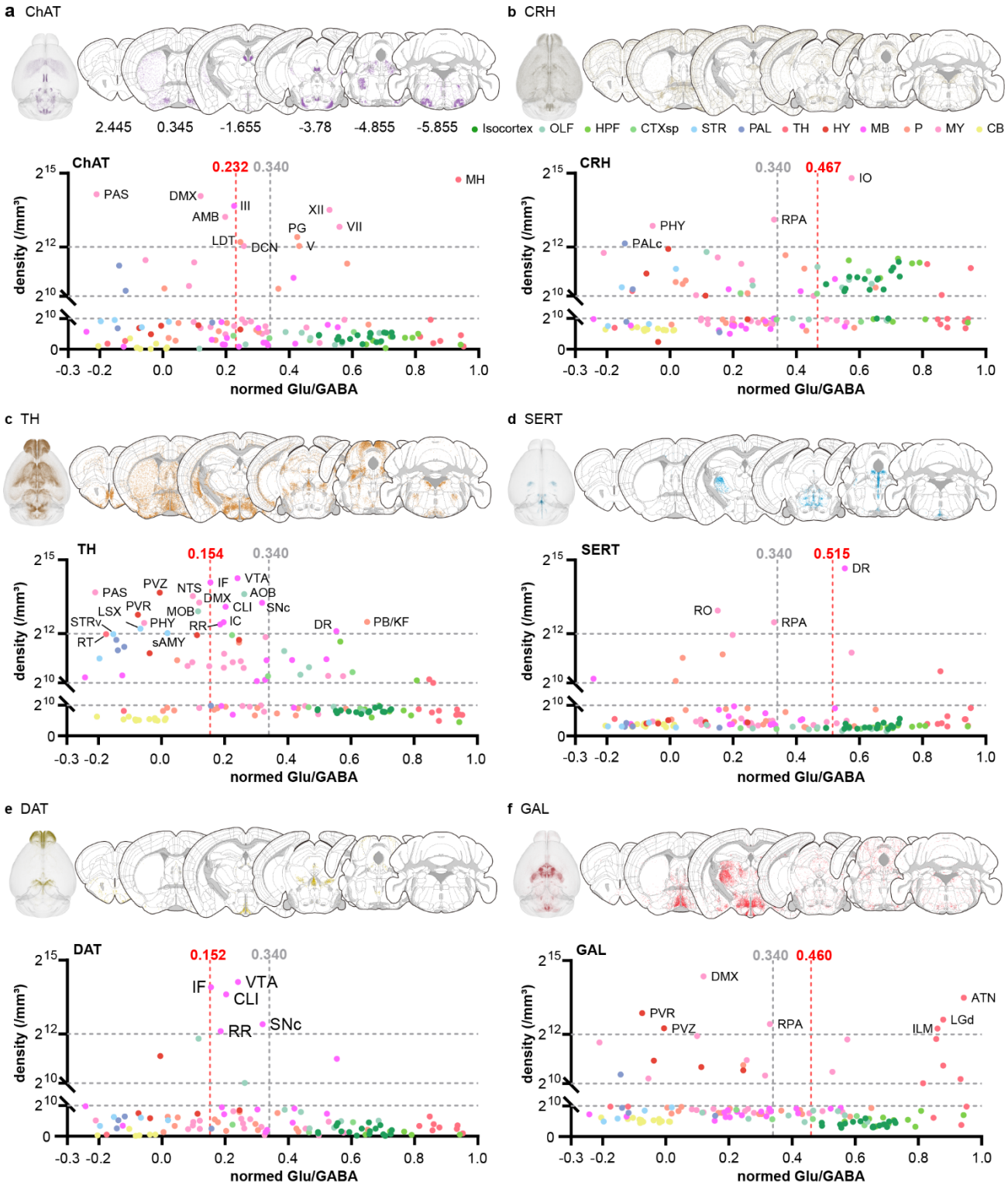

Supplementary Fig. 12 | Spatial distributions of modulatory neurons and their relationships with normed Glu/GABA in 134 brain regions

(a-f) Upper: 3D views and representative coronal slices showing the whole-brain distribution of 6 types of modulatory neurons. Distances from bregma for each coronal slice are indicated below, with all dimensions in millimeters. Lower: The relationship between the densities of each type of modulatory neuron and normed Glu/GABA across 134 brain regions. The grey dashed lines represent

the mean values of normed Glu/GABA in these regions, while the red dashed lines indicate the Modulatory normed Glu/GABA (Methods) for each type of neuron.

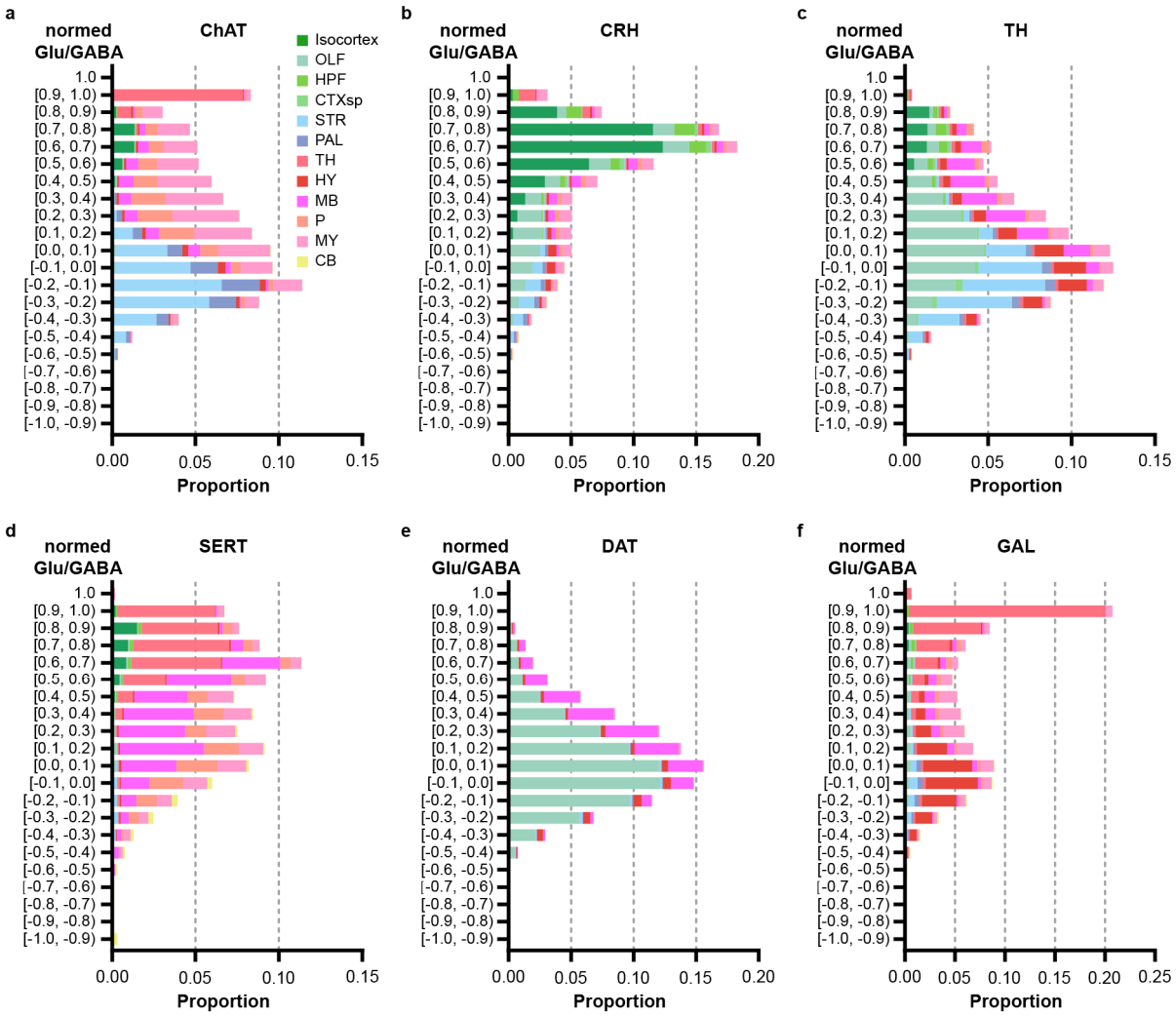

Supplementary Fig. 13 | Cubic analysis of the distribution of 6 types of modulatory neurons vs. normed Glu/GABA

(a-f) Cumulative proportions of neurons within each range of normed Glu/GABA. Colors represent the 12 brain regions to which each cube belongs.

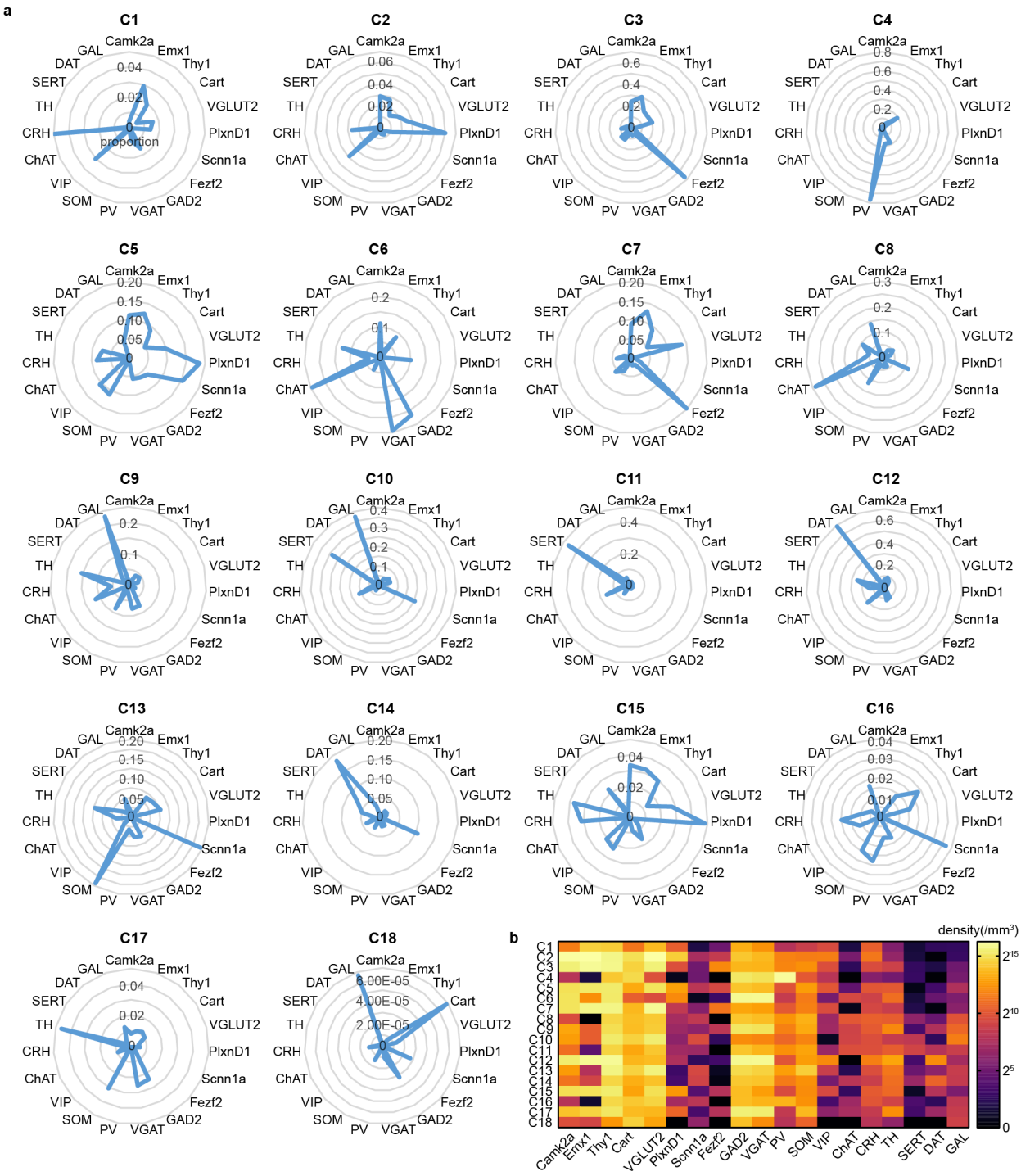

Supplementary Fig. 14 | Relationships between the distribution of 19 types of neurons and the 18 clusters in the first clustering of the whole brain

(a) Proportions of different neuron types across the 18 clusters.

(b) Heatmap of neuronal density for different neuron types within the 18 clusters.

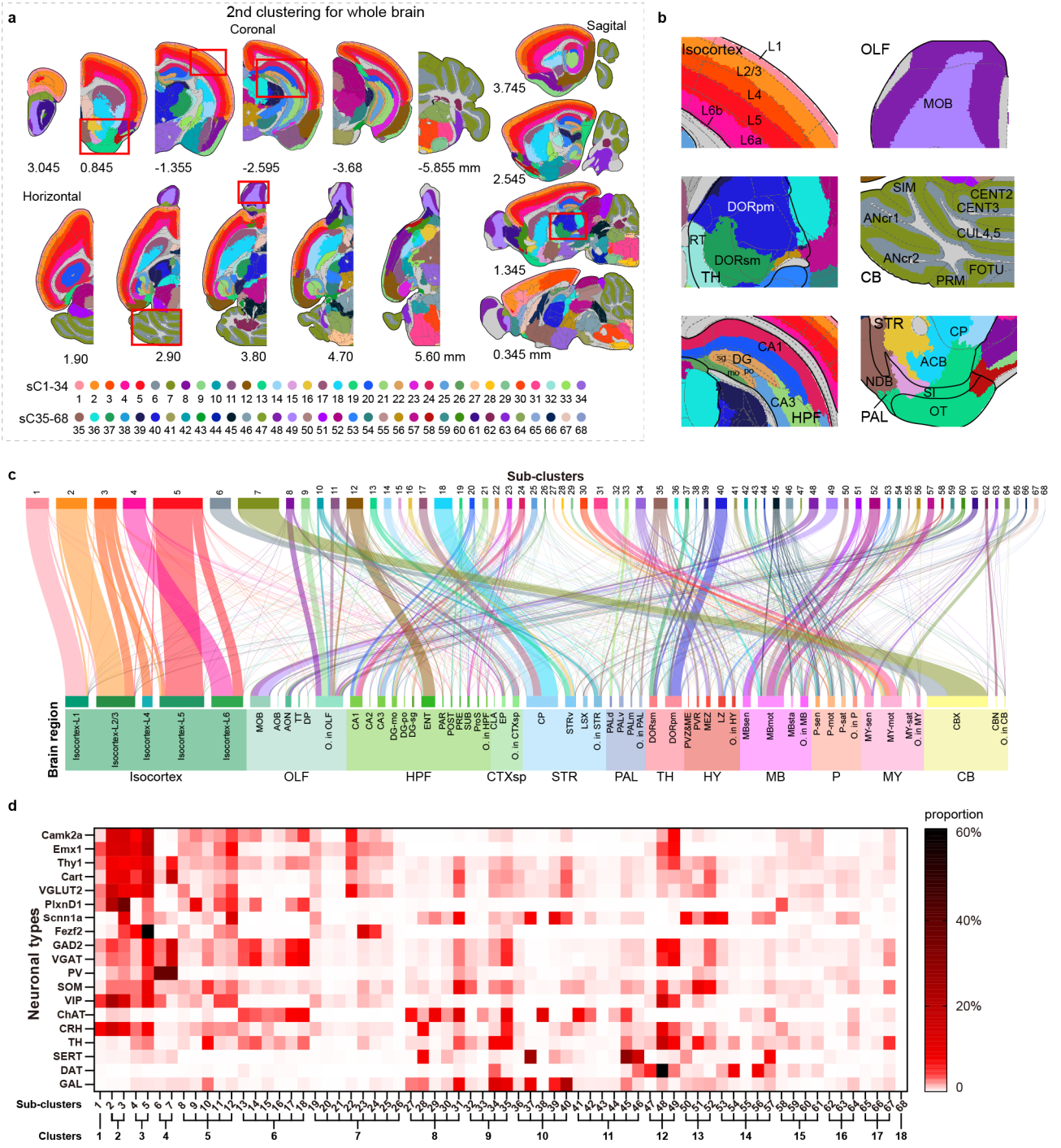

Supplementary Fig. 15 | The second clustering results of the whole brain and relationships between the distribution of 19 types of neurons and 68 sub-clusters

(a) Visualization of clustering results in coronal, horizontal, and sagittal planes. Distances from bregma for coronal planes, from the midline for sagittal planes, and from the dorsal surface of the Allen CCFv3 mouse brain are shown below. All dimension units are in millimeters. sC, sub-cluster.

(b) Enlarged views from (a) comparing clustering results with anatomical boundaries.

(c) Volume proportions of 68 sub-clusters in 57 anatomical brain regions.

(d) Heatmap of the proportions of different neuron types in 68 sub-clusters.

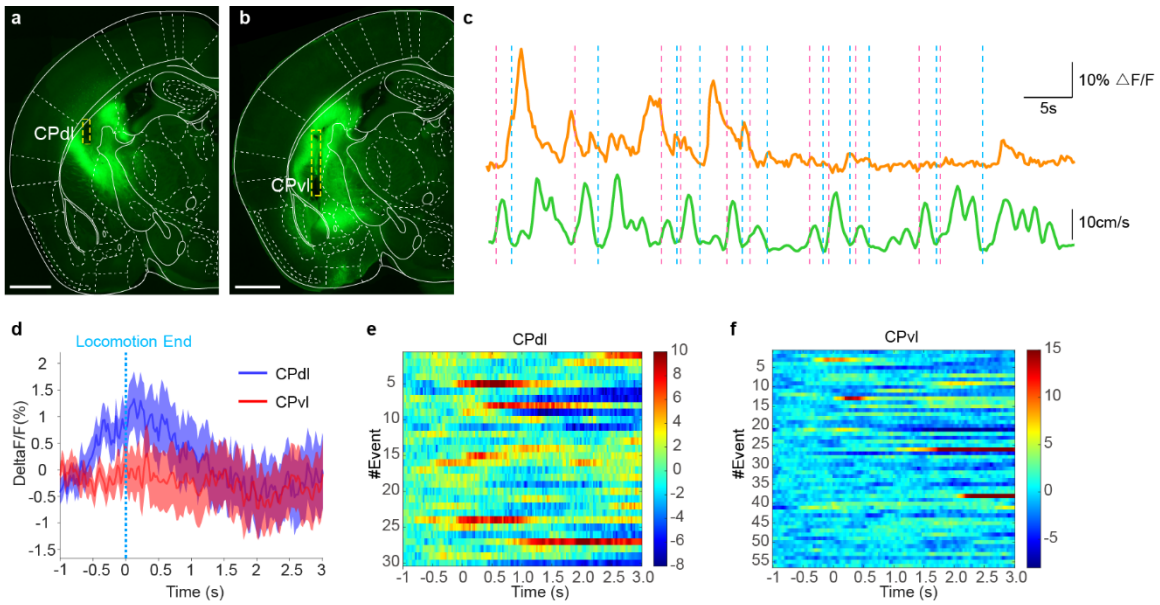

Supplementary Fig. 16 | Functional experiments in CPdl and CPvl

(a-b) Representative images showing the virus injection sites and the position of the optical fiber for CPdl and CPvl, respectively. Scale bar, 1 mm.

(c) A representative trace of the transient calcium signal of glutamatergic neurons in CPdl (orange) and the corresponding mouse speed (green).

(d) Average plots from individual animals showing differential calcium response activity of glutamatergic neurons in CPdl and CPvl during locomotion end events.

(e-f) Heatmaps of calcium transients in glutamatergic neurons during locomotion end events in CPdl (e) and CPvl (f), respectively.

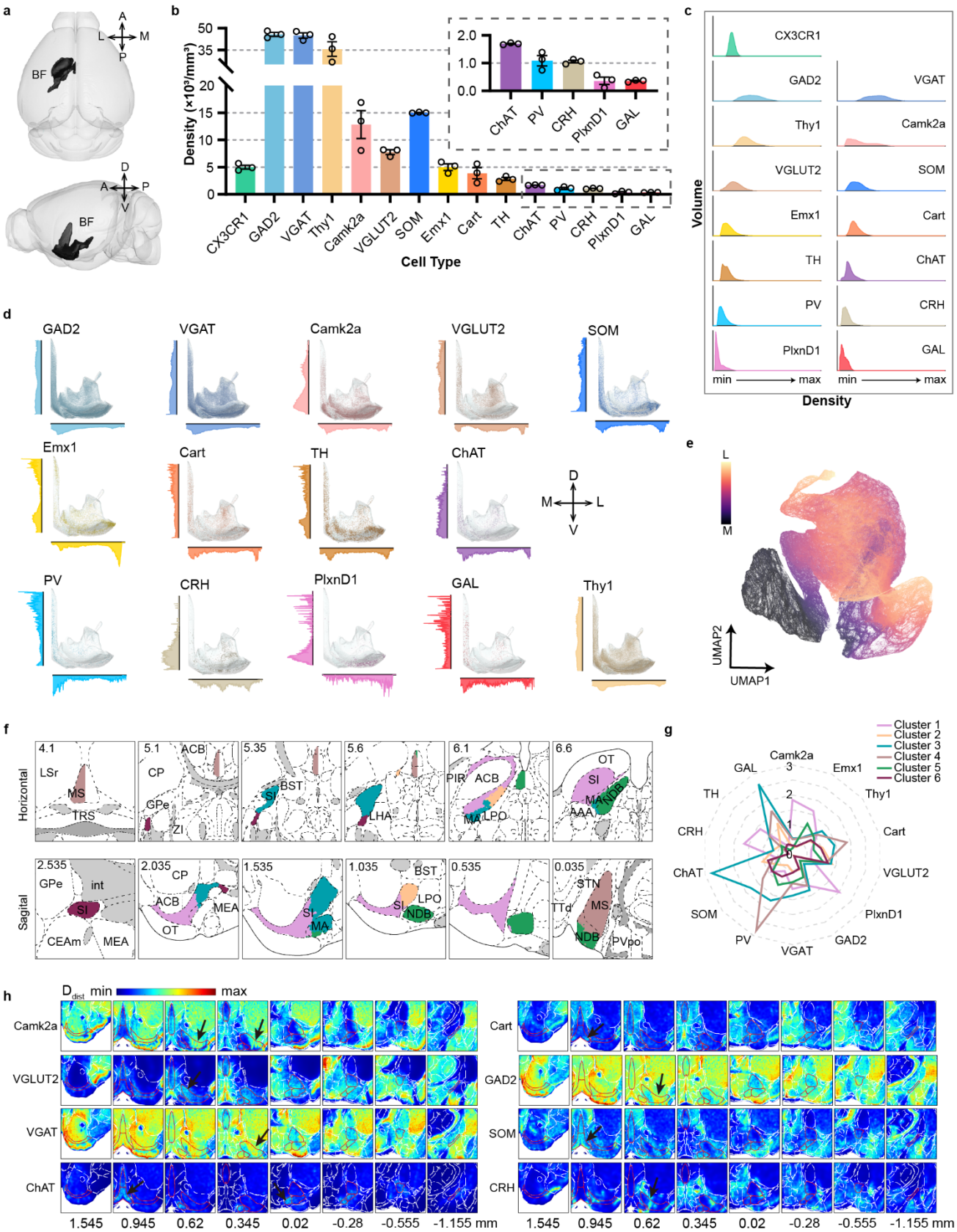

Supplementary Fig. 17 | Molecularly defined subregions in BF

(a) Spatial location of the BF in the mouse brain.

(b) Quantification of different types of cells in the BF.

(c) Distribution of volume and density of different cell types in the BF.

(d) 3D views of 13 types of neurons in the BF, with their density distributions along the AP and ML axes shown on the left and below for each type, respectively.

(e) UMAP representation of all data cubes in the BF, colored by their positions along the AP axis.

(f) Horizontal (upper) and sagittal (lower) views of subregions in the BF, colored by clusters and their adjacent brain regions. Distances from the top of the brain and the midline are shown in the upper left.

(g) Radar chart of clusters and cell density distribution in the BF. The density in each cluster is normalized by dividing by the average density in the BF for each cell type.

(h) Heatmap of neuronal density for different cell types in the BF. Discriminative distributions are indicated by arrows. Distances from Bregma are shown below.

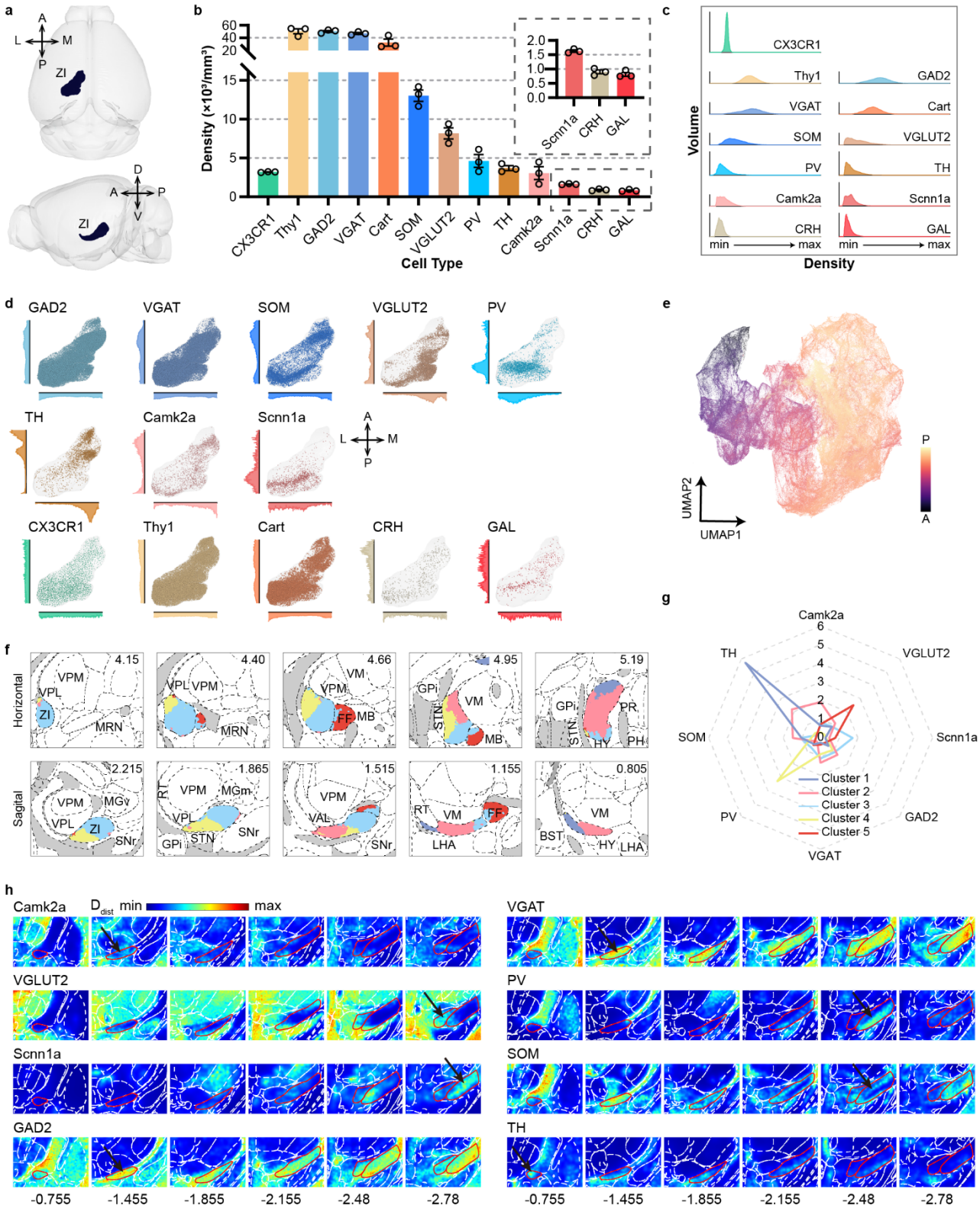

Supplementary Fig. 18 | Molecularly defined subregions in ZI

(a) Spatial location of the ZI in the mouse brain.

(b) Quantification of different types of cells in the ZI.

(c) Distribution of volume and density of different cell types in the ZI.

(d) 3D views of 13 types of neurons in the ZI, with their density distributions along the AP and ML axes shown on the left and below for each type, respectively.

(e) UMAP representation of all data cubes in the ZI, colored by their positions along the AP axis.

(f) Horizontal (upper) and sagittal (lower) views of subregions in the ZI, colored by clusters and their adjacent brain regions. Distances from the top of the brain and the midline are shown in the upper right.

(g) Radar chart of clusters and cell density distribution in the ZI. The density in each cluster is normalized by dividing by the average density in the ZI for each cell type.

(h) Coronal heatmap of neuronal density for different cell types in the ZI. Discriminative distributions are indicated by arrows. Distances from Bregma are shown below.

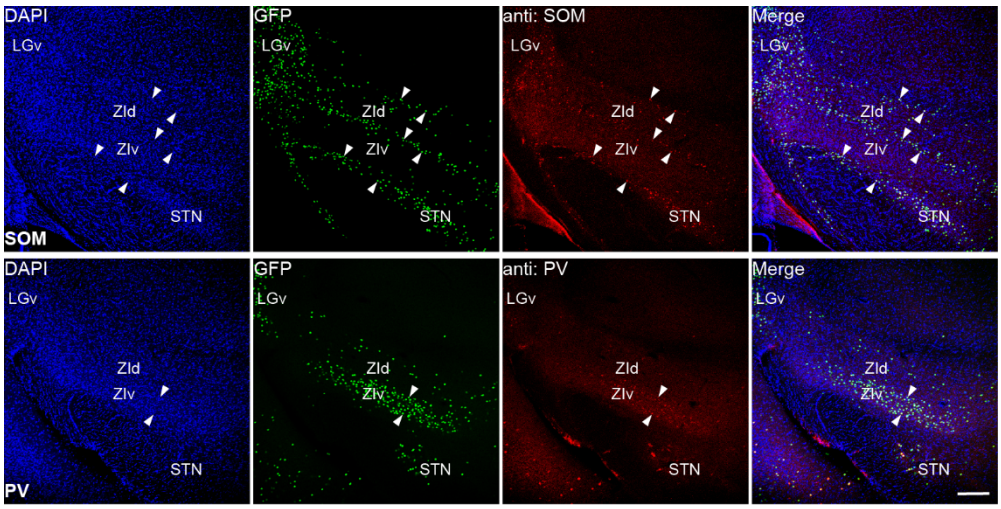

Supplementary Fig. 19 | IHC validation of SOM (upper) and PV (lower) neurons in ZI

Immunohistochemical staining of SOM-Crel;*LSL-H2B-GFP (upper) and PV-Cre;*LSL-H2B-GFP (lower) mice in the ZI. Scale bars, 200 µm.

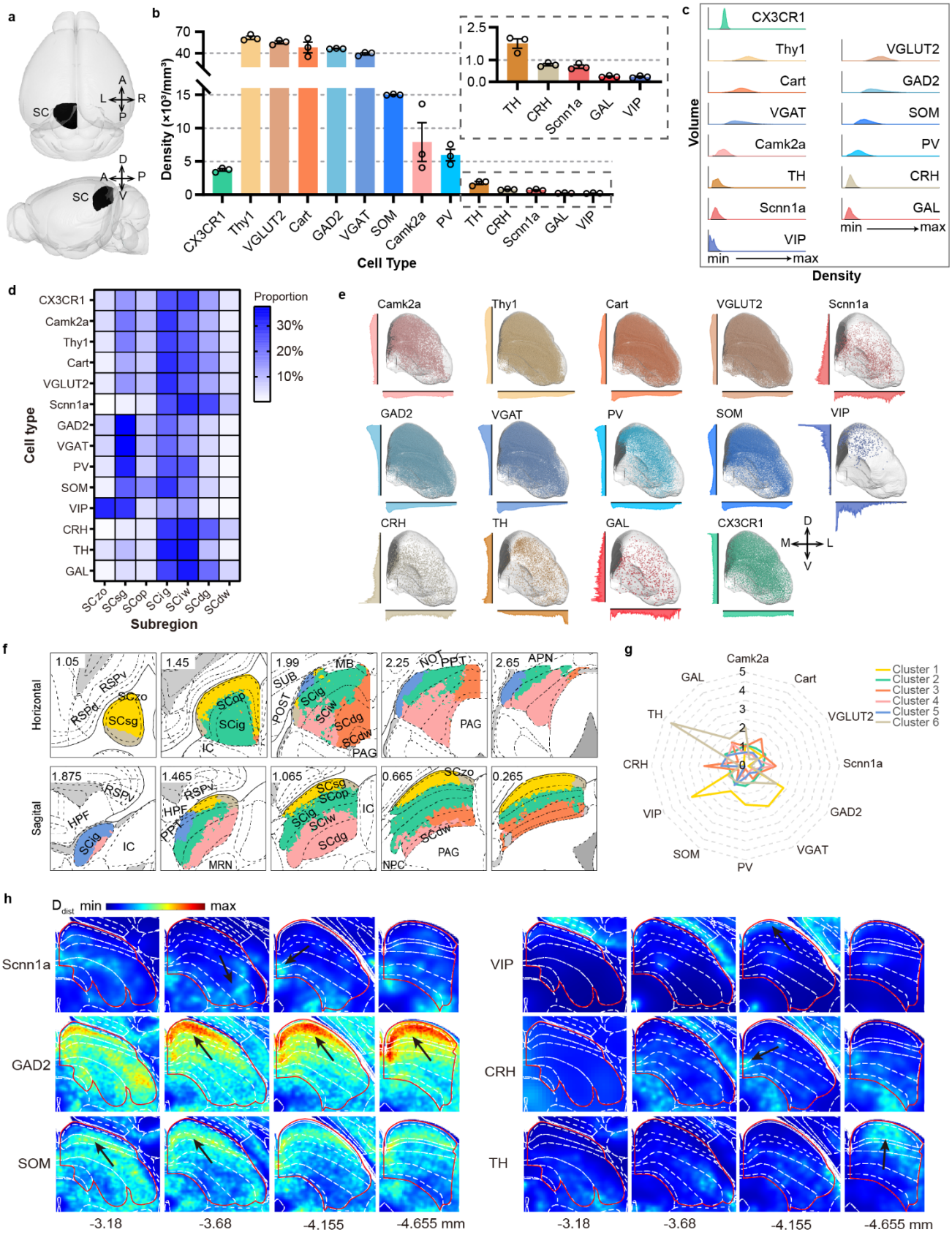

Supplementary Fig. 20 | Molecularly defined subregions in SC

(a) Spatial location of the SC in the mouse brain.

(b) Quantification of different types of cells in the SC.

(c) Distribution of volume with the density of different cell types in the SC.

(d) Proportional distribution of 13 neuron types across seven subregions of the SC.

(e) 3D views of 13 types of neurons in the SC and their density distributions along the AP and ML axes, shown on the left and below for each type.

(f) Horizontal (upper) and sagittal (lower) views of subregions in the SC, colored by clusters, along with their adjacent brain regions. Distances from the top of the brain and the midline are shown in the upper left.

(g) Radar chart illustrating cluster distribution and cell density in the SC. The density in each cluster is normalized by dividing by the average density in the SC for each cell type.

(h) Coronal heat map of neuronal density for different types in the SC. Distinctive distributions are indicated by arrows. Distances from Bregma are shown below.

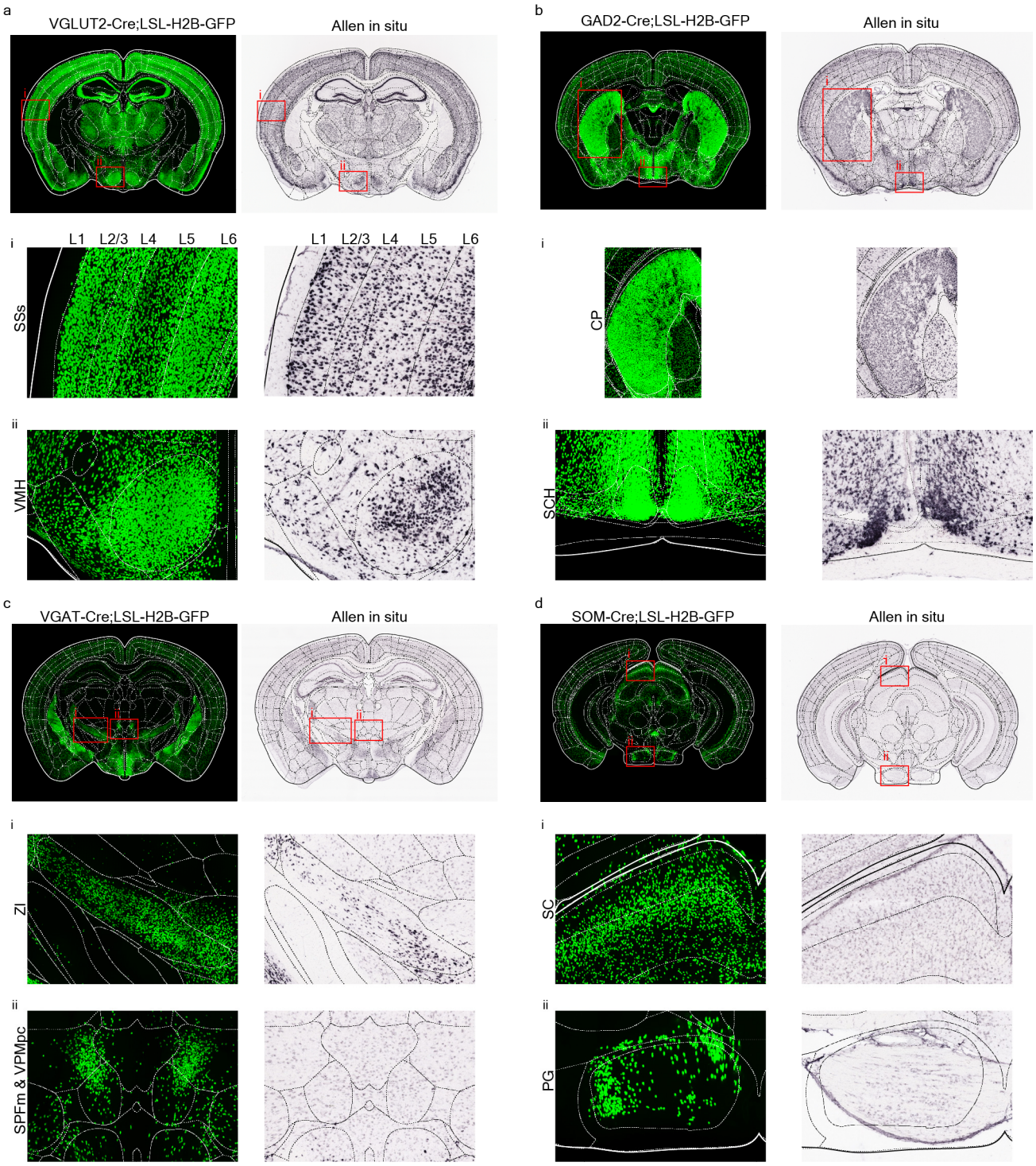

Supplementary Fig. 21 | fMOST data in comparison to Allen Brain In Situ Hybridization Data

(a) The density of VGLUT2$^+$ cells detected by fMOST imaging of VGLUT2-Cre$^+$ cells (first column of panels) is comparable to that detected by Allen in situ hybridization (second column of panels). The second row shows the density across layers of the supplemental somatosensory area (SSs), and the third row highlights the high density in the VMH region.

(b) The density of GAD2$^+$ cells detected by fMOST imaging of GAD2-Cre$^+$ cells (first column of panels) is comparable to that detected by Allen in situ hybridization (second column of panels). The second row illustrates the cell density in the CP, revealing density differences between the dorsal and ventral

areas, and the third row highlights the high density in the suprachiasmatic nucleus (SCH) region.

(c) The density of $VGAT^+$ cells reveals both similarities and differences when compared between fMOST imaging of $VGAT2^+$ cells (first column of panels) and Allen in situ hybridization (second column of panels). The second row shows similar densities in the ZI, while the third row highlights density differences in the magnocellular part of subparafascicular nucleus (SPFm) and parvicellular part of ventral posteromedial nucleus of the thalamus (VPMpc).

(d) The density of SOM^+ cells detected by fMOST imaging of SOM^+ cells (first column of panels) differs from that detected by Allen in situ hybridization (second column of panels). The second row illustrates density differences in the SC, and the third row shows differences in the PG.

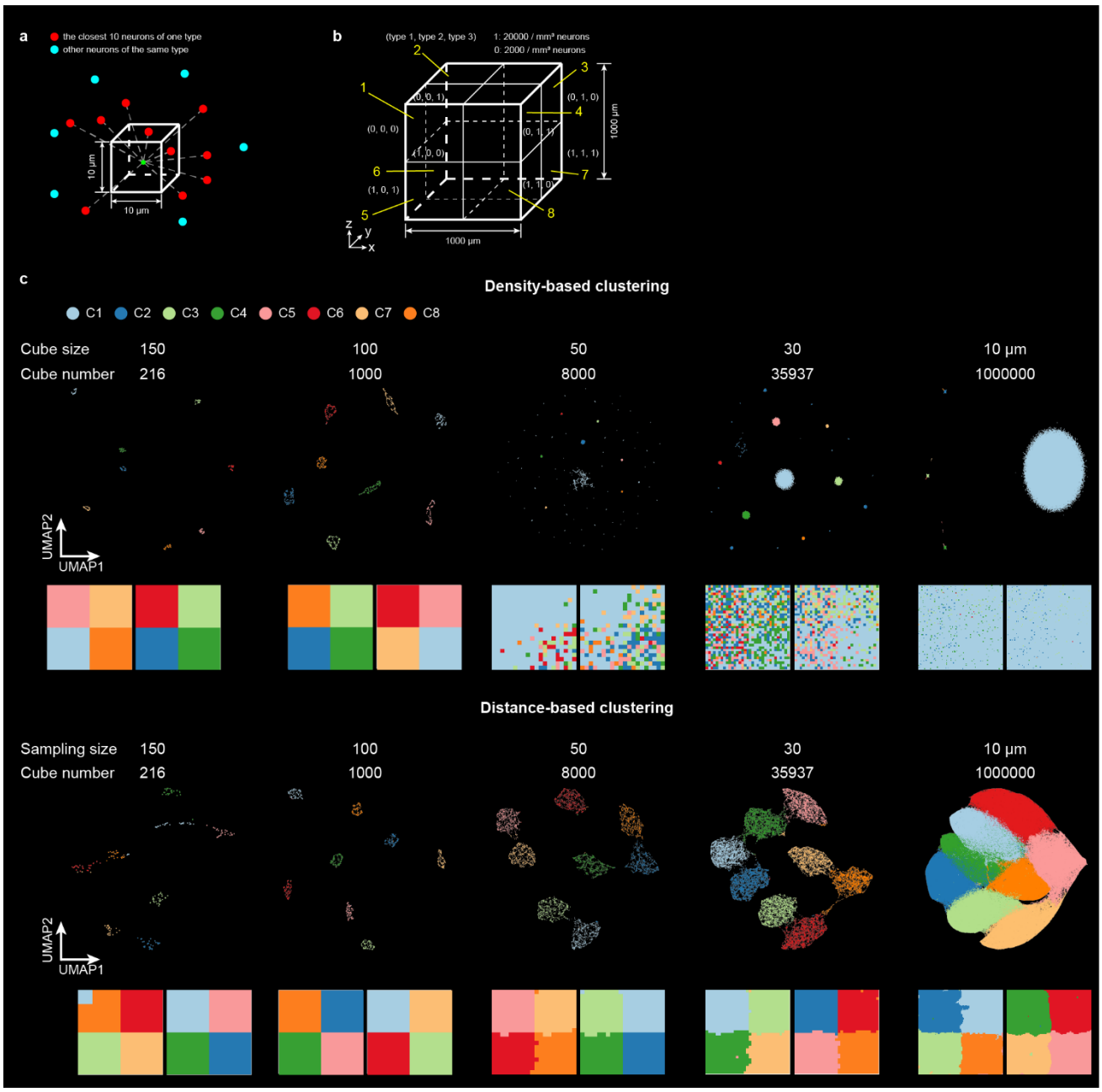

Supplementary Fig. 22 | Comparison of density-based and distance-based clustering

(a) The average distance from the 10 neurons nearby to the center of the cube (10 µm × 10 µm × 10 µm) is used to describe local distribution of neurons for each type. Red dots indicate the closest 10 neurons to the center of the cube (the green dot) of one type. Cyan dots indicate other neurons of the same type.

(b) A schematic diagram of a three-dimensional (3D) model of the distribution of neurons, which is a cube with a side length of 1000 µm. We assume that there are three different types of neurons, each with two distribution patterns of different densities (20000 / mm^3 and 2000 / mm^3) in different regions of the 3D model. The whole model is divided into 8 equally large regions (500 µm × 500 µm × 500 µm for each) with different neuron composition patterns. In each divided region, each type of neuron is randomly distributed in space with a corresponding density.

(c) UMAP representations and representative parallel sections of the 3D model colored by clusters (Methods) with different cube sizes (150 μm, 100 μm, 50 μm, 30 μm, 10 μm indicates the length of side of each cube) of neuronal density data and different sampling sizes (sampling points are taken every 150 μm, 100 μm, 50 μm, 30 μm, 10 μm for three orthogonal directions) of neuronal distance data. The number of cubes in each case is shown at the top of the UMAP.